Analysis of phonon decay processes in corundum structured α-In_2O_3 and α-Al_2O_3 by temperature dependent Raman spectroscopy

Elias Kluth [*,†], Josephin E. Müller [*] and Rüdiger Goldhahn

Institut für Physik, Otto-von-Guericke-Universität Magdeburg, Universitätsplatz 2, 39106 Magdeburg, Germany

Akito Taguchi and Tomohiro Yamaguchi

Department of Applied Physics, School of Advanced Engineering, Kogakuin University, 2665-1 Nakano, Hachioji, Tokyo 192-0015, Japan

Martin Feneberg

Institut für Physik, Otto-von-Guericke-Universität Magdeburg, Universitätsplatz 2, 39106 Magdeburg, Germany

(Received 11 March 2026; accepted 16 June 2026; published 31 July 2026)

Temperature dependent Raman spectroscopy was employed on α-In_2O_3 and α-Al_2O_3 to determine the phonon decay factors associated with the decay of phonons into two and three phonons. Differently oriented corundum structured α-In_2O_3 and α-Al_2O_3 samples were analyzed by temperature dependent Raman spectroscopy between 80 and 300 K. The shift of the resonance frequency of the Raman active phonon modes $A_{1g}(1)$, $E_g(4)$, and $E_g(5)$ was investigated by a model function including the thermal expansion of the lattice and the decay of the phonons into two and three phonons with lower energy. We obtain the phonon decay factors A and B representing the decay into two and three phonons, respectively. The findings are in reasonable agreement with the existing literature on α-Al_2O_3, α-Ga_2O_3, and α-In_2O_3.

DOI: 10.1103/vxv3-wrh3

I. INTRODUCTION

The semiconductor In_2O_3 has long been established in modern electronics as a transparent conductive oxide (TCO), especially in its combination with Sn [indium-tin-oxide (ITO)] [1–6]. Widespread applications reach from transparent conductive windows [7,8] over thin film transistors [9–11], Schottky contacts [12,13], solar cells [1,14,15], and gas sensing devices [16] to light emitting diodes (LEDs) [17] and lasers [18]. In applications, and hence in research, mainly the stable cubic bixbyite structure ($Ia\bar{3}$) of In_2O_3 is of interest [2,19–31].

But like other semiconductor oxides (e.g., Ga_2O_3 or Al_2O_3), In_2O_3 is a polymorph, with at least four metastable crystal phases. Besides an additional cubic ($I2_13$) and the two orthorhombic (*Pbcn* and *Pnma*) phases [7,32,33], the metastable phase, with the highest potential in future applications, is certainly the rhombohedral corundum structured α-phase ($R\bar{3}c$). Its crystal structure is the stable phase of sapphire, i.e., corundum (α-Al_2O_3). α-Al_2O_3 itself is, besides a few applications in ceramics [34,35], mainly used as substrate for other semiconductors like GaN [36,37] or α-Ga_2O_3 [38,39]. Due to its phase matching with α-Al_2O_3 and α-Ga_2O_3, α-In_2O_3 offers the possibility of band-gap engineering by alloying [40,41] over a range from 3.38 (direct band gap of α-In_2O_3 [42]) to 9.2 eV (direct band gap of α-Al_2O_3 [43]). The corundum structure is hereby the only phase, which exists in all three group-III sesquioxides [7]. While there is an increasing interest into the corundum structured Group-III-oxide alloy system [44–46], also alloying with other transition metal sesquioxides in the corundum α-phase like α-Fe_2O_3, α-Cr_2O_3, α-Ti_2O_3 [40,47] or α-Ir_2O_3, especially because of its potential in *p*-type doping [48–50], is of interest. There are a variety of theoretical studies regarding α-In_2O_3 [33,51–53], along with research on the growth [54–56], whereby mist chemical vapor deposition (mist CVD) seems to be emerging as the most promising method in terms of single crystal growth [57–60].

Experimental studies on the optical properties especially the phonon behavior of α-In_2O_3 are rare. In an earlier study we examined the dielectric function (DF) from the infrared (IR) to the ultraviolet (UV) spectral range, including the IR active phonon modes of the ordinary DF, accompanied by Raman spectroscopy to determine the polarization dependence of the Raman active phonon modes [42]. Additionally García-Domene *et al.* [61] investigated the Raman active phonon modes at high pressure up to 30 GPa. Phonon properties, specifically the anharmonicity, is known to play a relevant role in the reduction of the thermal conductivity [62,63]. One way to examine the anharmonic phonon behavior is by temperature dependent Raman spectroscopy. In a previous investigation we explored the anharmonicity of selected phonon modes in α-Ga_2O_3 [$A_{1g}(1)$ and $E_g(2)$ mode] and α-Al_2O_3 [$A_{1g}(1)$ and

*These authors contributed equally to this work.
†Contact author: elias.kluth@ovgu.de

Published by the American Physical Society under the terms of the Creative Commons Attribution 4.0 International license. Further distribution of this work must maintain attribution to the author(s) and the published article's title, journal citation, and DOI.

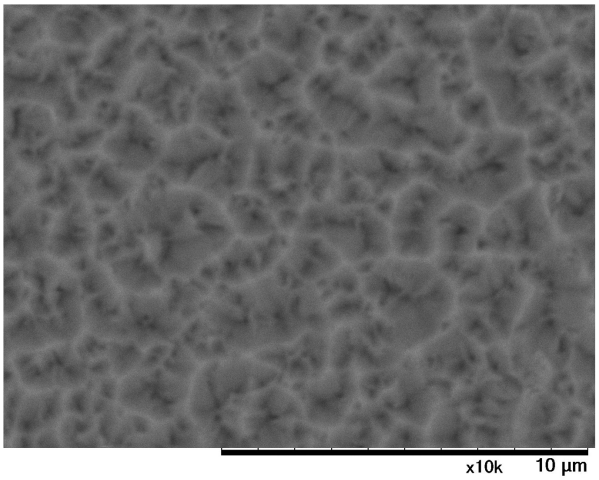


FIG. 1. Surface morphology measured by SEM of the α-In_2O_3 film of sample S2.

$E_g(1)$ mode] [64]. Then, recently Cuscó *et al.* [65] reported on the temperature dependent behavior of both A_{1g} phonon modes in α-In_2O_3.

In this work, we employ temperature dependent Raman spectroscopy on α-In_2O_3 and additionally on α-Al_2O_3. Other than in the existing literature, Raman spectroscopy along different orientations of α-In_2O_3 and α-Al_2O_3, parallel and perpendicular to the c-axis, is investigated. In addition to A_{1g} modes, also the temperature dependent behavior of selected E_g modes is evaluated. Similar to an earlier study on α-Ga_2O_3, we employ a model including the thermal expansion of the lattice and the decay of the phonons into two and three phonons with lower energy. While the only previous results on the temperature behavior of phonons in α-In_2O_3 by Cuscó *et al.* [65] focused on the anharmonic behavior, our model approach led to the determination of the phonon decay factors A and B, which are then compared to the earlier results on α-Ga_2O_3 [64].

II. EXPERIMENTAL AND THEORY

For the α-Al_2O_3 (sapphire) samples of this study, commercially available (0001) (c-plane) and (10$\bar{1}$0) (m-plane) α-Al_2O_3 wafer were used. The corundum structured (0001) α-In_2O_3 samples were grown on (0001) α-Al_2O_3 substrate by mist CVD. In_2O_3 powder was used as a precursor by dissolving it in HCl solution. The mist particles were formed by a 2.4 MHz ultrasonic transducer. They were then carried by a flow of O_2 gas to the reaction chamber, which was heated to 550 °C. The α-In_2O_3 layer thickness of the two samples used in this study was determined by spectroscopic ellipsometry to be 2.2 and 4 µm. Exemplary surface morphology of the α-In_2O_3 film of sample S2 measured by scanning electron microscopy (SEM) is displayed in Fig. 1. Further sample characteristics determined by Hall effect measurements and x-ray diffraction (XRD) can be found in Table I. More details on the growth process can be found elsewhere [59,60].

Raman spectroscopy was excited by a frequency double YAG:Nd laser ($\lambda = 532$ nm, max. $P \approx 20$ mW at the sample) in a Raman microscope (Olympus BX51) using a Mitutoyo

TABLE I. Layer thickness from spectroscopic ellipsometry, carrier density n, and mobility µ by Hall effect measurements and lattice parameters a and c from x-ray diffraction for the α-In_2O_3 samples.

Sample	Thickness (µm)	n (cm^{-3})	μ ($\frac{cm^2}{Vs}$)	a (Å)	c (Å)
S1	4.0	5.3×10^{17}	255	5.4852	14.5014
S2	2.2	8.2×10^{18}	107	5.4880	14.4912

×50 long working distance (LWD) objective. As spectrometer, an S&I TriVista 777 was employed (1800 lines/mm), with the entrance slit set to 100 µm for the α-In_2O_3 and m-plane α-Al_2O_3 measurements and to 200 µm for the c-plane α-Al_2O_3 measurements. For low temperatures, we used a liquid N_2 cooled cryostat (CryoVac) and a resistive heater (CryoVac TIC500), allowing temperature control between 80 and 300 K. Measurements were performed in backscattering geometry along the (0001) and (10$\bar{1}$0) direction for α-Al_2O_3 as well as for α-In_2O_3. Other than for α-Al_2O_3, in the case of α-In_2O_3 no m-plane samples were available. Therefore, measurements along the (10$\bar{1}$0) direction were performed on the edge of the sample. For this an adjustable micrometer stage was mounted underneath the cryostat to ensure proper alignment of the microscope onto the α-In_2O_3 layer. The setup is equipped with a polarizer and an analyzer. To maximize the signal intensity, the analyzer was removed in this study. The polarizer was fixed. The orientation of the measurements is given in Porto notation [67], e.g., $z(x,-)\bar{z}$, whereby $z \parallel c$ and $x \parallel m$. Accordingly, $x(y,-)\bar{x}$ refers to a measurement along the m-direction (10$\bar{1}$0), an edge measurement in the case of α-In_2O_3. The dash on the third position of the Porto notation denotes the absence of the analyzer.

The space-group $R\bar{3}c$ of the corundum crystal structure yields 18 zone center optical phonon modes [68]:

$$\Gamma_{\text{opt.}} = \mathbf{2}\boldsymbol{A_{1g}} + 2A_{1u} + 3A_{2g} + 2A_{2u} + \mathbf{5}\boldsymbol{E_g} + 4E_u \quad (1)$$

out of which the $2A_{2u}$ and $4E_u$ are infrared active and the $2A_{1g}$ and $5E_g$ are Raman active. Their room temperature characteristics in terms of resonance frequencies, polarization dependence, and relative intensities in comparison to theoretical calculations have been discussed already in an earlier study [42].

To analyze the phonon signals of the Raman spectra of the three most dominant phonon modes $A_{1g}(1)$, $E_g(4)$, and $E_g(5)$ [69] in c-plane α-Al_2O_3 and c-plane α-In_2O_3, they were fitted by a sum of Lorentzian line shapes:

$$I(\omega) = \frac{\tilde{A}}{\pi}\frac{\Gamma}{\Gamma^2 + (\omega - \omega_0)^2} \quad (2)$$

whereby $I(\omega)$ is the intensity of the Raman signal, $\tilde{A}$ is the amplitude, Γ is the broadening, with 2Γ being the FWHM, and ω_0 is the phonon frequency. Even though $A_{1g}(1)$, $E_g(4)$, and $E_g(5)$ are not the three most dominant signals anymore in m-plane α-Al_2O_3 and m-plane α-In_2O_3, these modes were selected to allow comparability to c-plane α-Al_2O_3 and c-plane α-In_2O_3.

To describe the temperature dependence of the phonon frequencies $\omega(T)$, two main effects have to be considered:

TABLE II. Grüneisen parameters γ for the different evaluated phonon modes of α-Al_2O_3 and α-In_2O_3 by García-Domene *et al.* [61] and the thermal expansion coefficient α of α-Al_2O_3 as 5th degree polynomial function by Grümbel *et al.* [64] based on data from Schauer [66].

	α-Al_2O_3			α-In_2O_3		
	$A_{1g}(1)$	$E_g(4)$	$E_g(5)$	$A_{1g}(1)$	$E_g(4)$	$E_g(5)$
γ [61]	1.15	1.28	1.52	0.92	2.15	1.77
α (K^{-1}) [64,66]	$-3.60122 + 0.05103\ T - 9.3857 \times 10^{-5}\ T^2$ $+9.1846 \times 10^{-8}\ T^3 - 4.51844 \times 10^{-11}\ T^4$ $+8.87347 \times 10^{-15}\ T^5$					

(1) the thermal expansion (e) of the lattice, and (2) the decay (d) of the phonons into phonons having lower frequency, i.e., energy [70]:

$$\omega(T) = \omega_0 + \Delta\omega_e(T) + \Delta\omega_d(T). \tag{3}$$

The thermal expansion contribution $\Delta\omega_e(T)$ is dependent on the Grüneisen parameter γ and the thermal expansion coefficients of the corundum lattice, which is parametrized in hexagonal form as $\alpha_\perp$ and $\alpha_\parallel$ [70]:

$$\Delta\omega_e(T) = -\omega_0\gamma \int_0^T [2\alpha_\perp(T') + \alpha_\parallel(T')]dT' \tag{4}$$

The Grüneisen parameter γ is not only dependent on the material but also on the specific phonon modes. A mode Grüneisen tensor by García-Domene *et al.* [61] was used. The Grüneisen parameter is approximated to not be temperature dependent itself in the framework of this study, as we expect intrinsic temperature variation of the Grüneisen parameter to be small compared with the dominant effects to the wave-number shift, the lattice expansion, and the phonon decay. Additionally, no temperature dependent Grüneisen parameters are applicable yet from the literature. For the thermal expansion coefficient, an isotropic averaged $\alpha = \alpha_\perp = \alpha_\parallel$ polynomial of 5th degree by Grümbel *et al.* [64] (developed for α-Al_2O_3 based on data by Schauer [66]) was taken for both α-Al_2O_3 and α-In_2O_3, as comparable temperature dependent thermal expansion coefficients for α-In_2O_3 are not yet available. Bixbyite-In_2O_3 values were tested but deemed not suitable. All values/functions used are listed it Table II.

The phonon decay contribution $\Delta\omega_d(T)$ is described by the eigenfrequency of the anharmonic Hamiltonian H_A. The total vibrational Hamiltonian H can be written as $H = H_0 + H_A$ with the harmonic Hamiltonian H_0. We presume symmetric decay of zone-centered phonons and take into account cubic (H') and quartic (H'') corrections to H_0 in perturbation theory, i.e., $H_A = H' + H''$. This describes a decay into two phonons with $\omega = \frac{\omega_0}{2}$ and three phonons with $\omega = \frac{\omega_0}{3}$. For the frequency shift $\Delta\omega_d(T)$, this leads to [70,71]

$$\Delta\omega_d(T) = A\left[1 + 2n\left(T, \frac{\omega_0}{2}\right)\right] + B\left[1 + 3n\left(T, \frac{\omega_0}{3}\right) + 3n^2\left(T, \frac{\omega_0}{3}\right)\right] \tag{5}$$

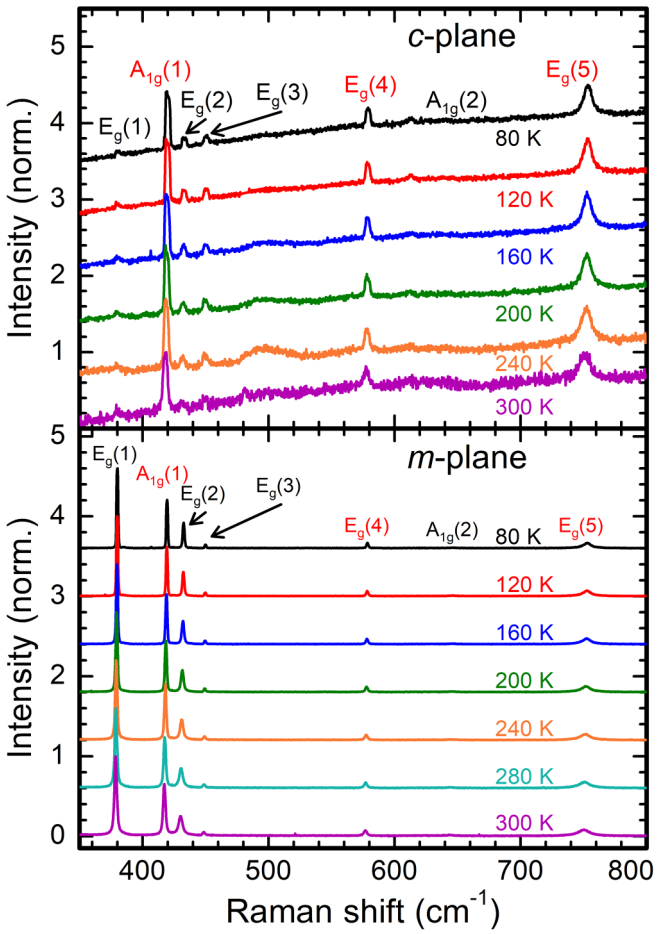


FIG. 2. Temperature-dependent Raman spectra of *c*-plane α-Al_2O_3 (upper panel) and *m*-plane α-Al_2O_3 (lower panel) in $z(x,-)\bar{z}$ and $x(y,-)\bar{x}$ configuration, respectively. All spectra are normalized separately to their maximum intensity and vertically offset for clarity. Red marked phonon modes were chosen for further evaluation.

with the bosonic occupation factor

$$n(T,\omega) = \frac{1}{e^{\hbar\omega/k_BT} - 1}. \tag{6}$$

A and B are the phonon decay factors of the decay into two and three phonons, respectively.

III. RESULTS AND DISCUSSION

A. α-Al_2O_3

Temperature dependent Raman spectra from 80 to 300 K of *c*-plane and *m*-plane α-Al_2O_3 are displayed in Fig. 2. The spectra taken from *m*-plane α-Al_2O_3 show a noticeable higher signal-to-noise ratio than those from *c*-plane, even though a higher measurement time and slit entrance was chosen for the latter. This is probably due to different Raman tensor ($\boldsymbol{R}$) elements of α-Al_2O_3 which relate to the signal intensity I_s as $I_s \sim |\vec{e}_L\ \boldsymbol{R}\ \vec{e}_S|^2$ [with $\vec{e}_L$ and $\vec{e}_S$ being the polarization state of the incident laser (L) light and scattered (S) light, respectively]. The tensor elements governing measurements along the $z(x,-)\bar{z}$ orientation lead to lower I_s than the ones along

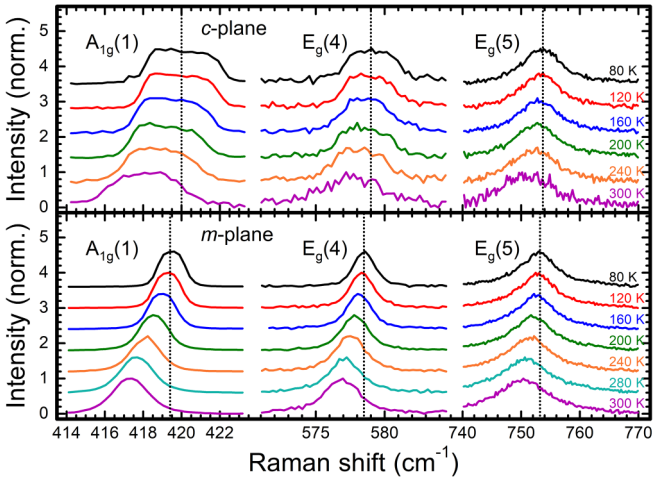


FIG. 3. Cutouts of the temperature-dependent Raman spectra of c-plane α-Al_2O_3 (upper panel) and m-plane α-Al_2O_3 (lower panel) in $z(x,-)\bar{z}$ and $x(y,-)\bar{x}$ configuration, respectively. The region of the phonon modes marked red in Fig. 2, $A_{1g}(1)$ (left) $E_g(4)$ (middle) and $E_g(5)$ (right), are displayed. All spectra are normalized separately to their maximum intensity and vertically offset for clarity. A black dashed line marks the resonance wave number of the corresponding phonon mode at 80 K.

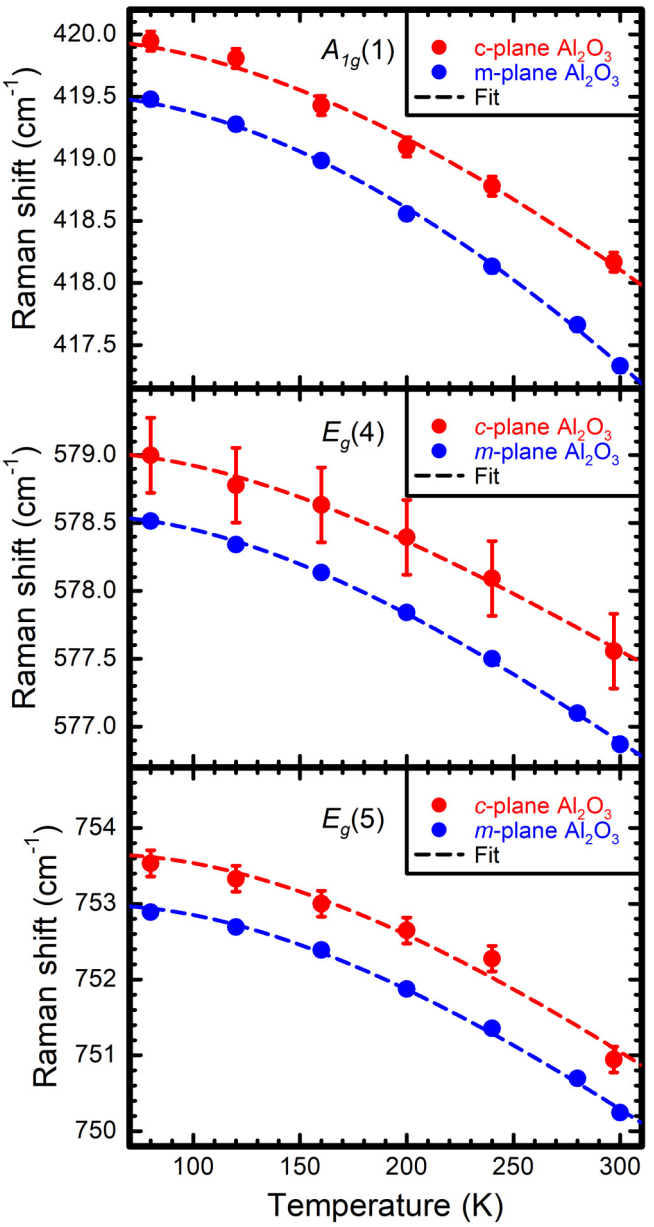


FIG. 4. Temperature-dependent shifts of the resonance frequencies of the $A_{1g}(1)$ (upper panel), $E_g(4)$ (middle panel), and $E_g(5)$ (bottom panel) phonon modes of c-plane (red) and m-plane (blue) α-Al_2O_3 together with the corresponding model fits (dashed lines) based on Eqs. (3)–(6). The error bars indicate the uncertainty of the Raman shift obtained from the Lorentzian fit using Eq. (2) applied to the Raman spectra. Error bars are shown only when they exceed the symbol size. The uncertainty of the temperature values is smaller than the symbol size for all data points.

the $x(y,-)\bar{x}$ orientation for most phonon modes. All Raman active phonon modes are visible in Fig. 2, even though the $A_{1g}(2)$ mode has a very weak intensity. Magnified sections of the spectra near the phonon modes $A_{1g}(1)$, $E_g(4)$, and $E_g(5)$ are displayed in Fig. 3. A shift to lower wave numbers with increasing temperature is noticeable. The phonon mode resonance frequencies of these modes were obtained by fitting the spectra by Eq. (2). The shift of their resonance frequencies to lower wave numbers with increasing temperature is displayed in Fig. 4.

c-plane (red) and m-plane (blue) measurements show a similar shift, even though they are offset by $\sim$0.5 cm^{-1} for all modes. While the specific cause for this shift remains unclear, the most probable cause lies in the fact that different wafers were used for the two measurement series. In total, the $E_g(5)$ mode shows the strongest shift from 80 to 300 K of $\sim$2.5 cm^{-1} while the $E_g(4)$ has the weakest one of $\sim$1.6 cm^{-1}. The $A_{1g}(1)$ mode lies in between with a shift of $\sim$2.1 cm^{-1}. The temperature dependence of the phonon frequencies is fitted by the model (dashed line) based on Eqs. (3)–(6) whereby the parameters in Table II are used and the phonon decay factors A and B are the fitting parameters. As the model only describes $\Delta\omega$, the offset between the phonon frequencies of c-plane and m-plane measurements has no influence on A and B. The resulting phonon decay factors and their numerical errors from the model-fit in Fig. 4, are reported in Table III. They are compared and discussed to literature data and the results on α-In_2O_3 in Sec. III C.

B. α-In_2O_3

Temperature dependent Raman spectra from 80 to 300 K of c-plane and m-oriented α-In_2O_3 are displayed in Fig. 5, accompanied by magnified sections of the spectra near the phonon modes $A_{1g}(1)$, $E_g(4)$, and $E_g(5)$ in Fig. 6. Besides all Raman active phonon modes of α-In_2O_3 several phonon modes of the α-Al_2O_3 substrate are visible as well. They are marked by asterisks. Since α-In_2O_3 did show a much higher signal intensity in both orientations, than α-Al_2O_3 we used the smaller monochromator entrance slit (100 μm) for the c-plane and m-oriented measurements and were still able to obtain a higher number (12 instead of 7) of measurements in one temperature series. Both c-plane samples (S1 and S2) show

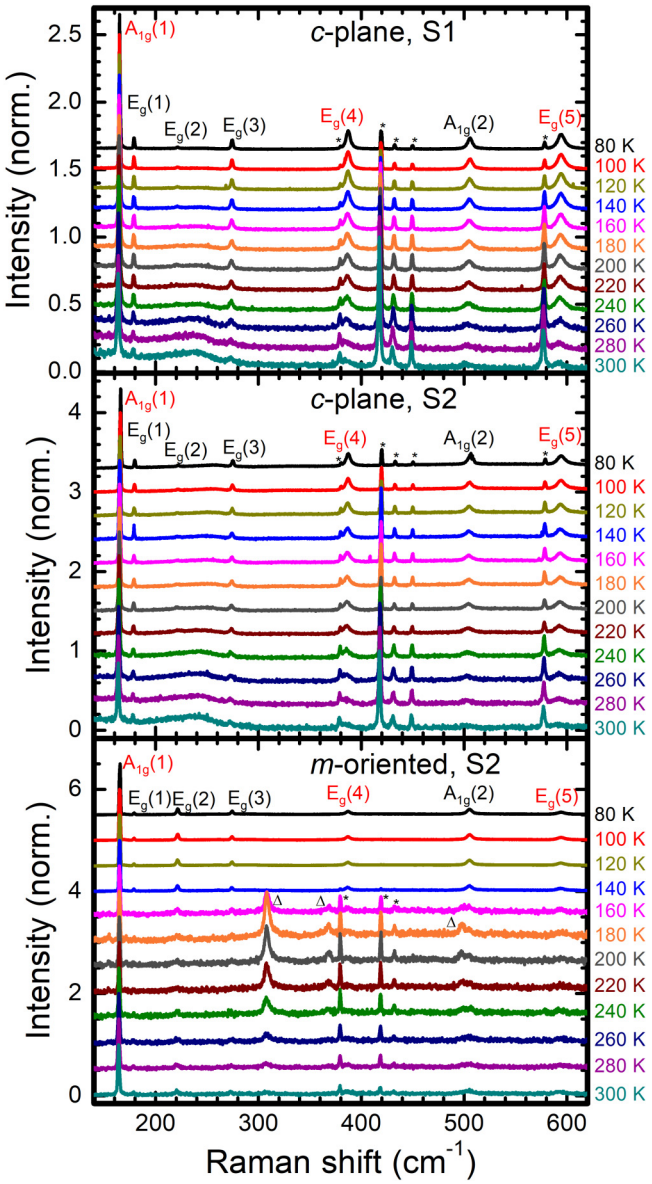


FIG. 5. Temperature-dependent Raman spectra of c-plane α-In_2O_3 (upper panel and middle panel, samples S1 and S2) in $z(x,-)\bar{z}$ configuration and m-oriented α-In_2O_3 (lower panel, sample S2, edge measurement) in $x(y,-)\bar{x}$ configuration. All spectra are normalized separately to their maximum intensity and vertically offset for clarity. Red marked phonon modes were chosen for further evaluation. Signals from the α-Al_2O_3 substrate are marked by an asterisk (*), while signals associated with cubic bixbyite-In_2O_3 are marked by Δ.

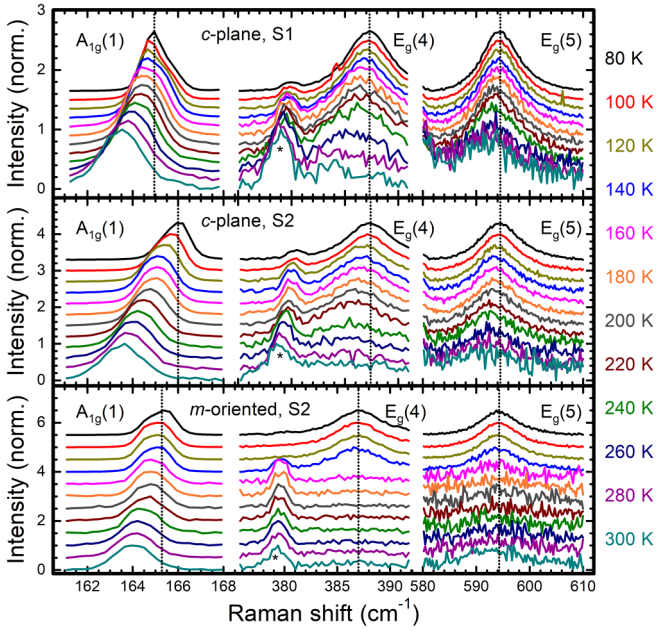


FIG. 6. Cutouts of the temperature-dependent Raman spectra of c-plane α-In_2O_3 (upper and middle panel, samples S1 and S2) and m-oriented α-In_2O_3 (lower panel, sample S2, edge measurement) in $z(x,-)\bar{z}$ and $x(y,-)\bar{x}$ configuration, respectively. The region of the phonon modes marked red in Fig. 5, $A_{1g}(1)$ (left) $E_g(4)$ (middle), and $E_g(5)$ (right), are displayed. All spectra are normalized separately to their maximum intensity and vertically offset for clarity. A black dashed line marks the resonance wave number of the corresponding phonon mode at 80 K. Signals from the α-Al_2O_3 substrate are marked by an asterisk (*).

similar results. The m-oriented measurements of sample S2, i.e., the measurements on the sample edge additionally depict three signals in the temperature range from 160 to 280 K which can be attributed to cubic bixbyite-In_2O_3 (marked by Δ) [72]. We explain the occurrence of bixbyite-In_2O_3 signals only in spectra taken at certain temperatures as follows: α-In_2O_3 is a metastable crystal phase. Therefore, to grow crystals completely free of cubic inclusions always remains a challenge, so these sample will include some cubic inclusions as well. Starting at 80 K with the measurement series the sample is heated up step-by-step to increase the temperature up to 300 K. In this process the sample expands, leading to a slight shift of our measurement spot on the sample. Obviously, our temperature series started at a position without any cubic inclusions, shifted between 160 and 280 K to a spot where inclusions are present and at higher temperatures further to a position without visible bixbyite contributions. As no such signals were found in any other measurements of these samples the cubic inclusions still seem to be reasonably small and few. For a similar reason, some of the m-oriented measurements show signals of the α-Al_2O_3 substrate, while others do not.

Here as well the signals of the $A_{1g}(1)$, $E_g(4)$, and $E_g(5)$ phonon modes were fitted using Eq. (2). The fit of the $E_g(4)$ and $E_g(5)$ modes, especially in the c-plane measurements, is hereby more complicated since the $E_g(1)$ and $E_g(4)$ modes of the α-Al_2O_3 substrate are closely adjacent, thus both signals (layer and substrate) always have to be fitted together. Fortunately, in the measurements on the sample edge this is less an issue since the α-Al_2O_3 signals are either not present at all or less pronounced than in the c-plane measurements.

The shift of the resonance frequencies of the $A_{1g}(1)$, $E_g(4)$, and $E_g(5)$ modes to lower wave numbers with increasing temperature for all three temperature series of α-In_2O_3 are displayed in Fig. 7. In contrast to the case of α-Al_2O_3 no clear systematic offset between c-plane and m-oriented measurements exists. It is noticeable though that the m-oriented

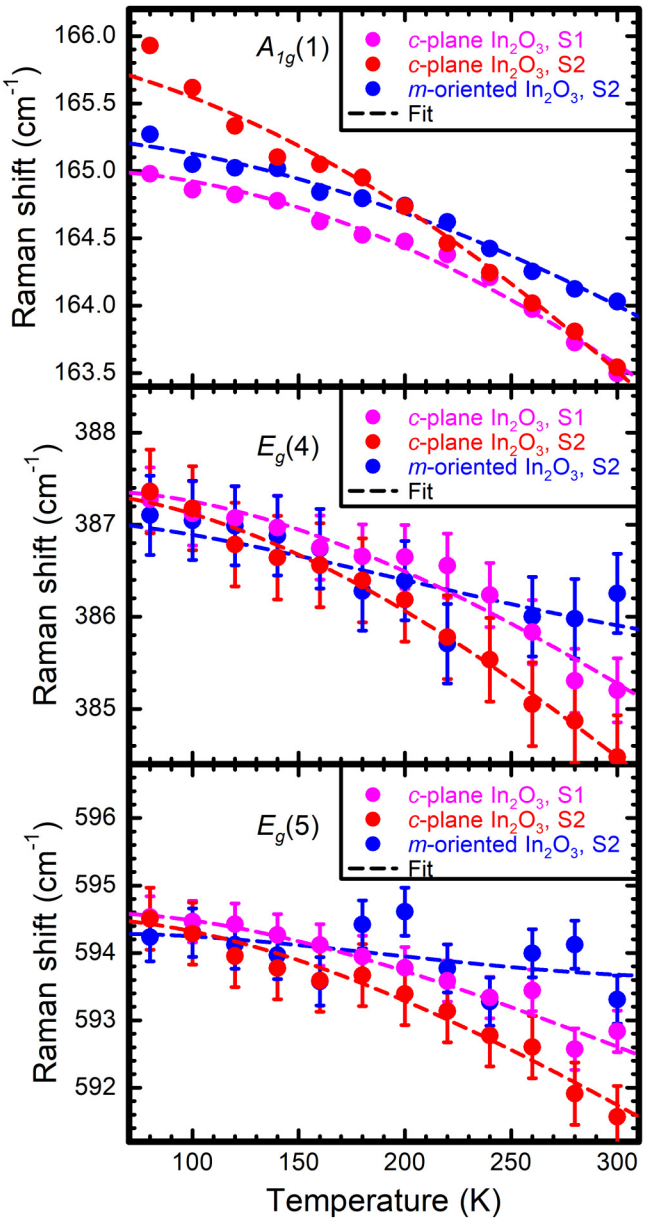


FIG. 7. Temperature-dependent shifts of the resonance frequencies of the $A_{1g}(1)$ (upper panel), $E_g(4)$ (middle panel), and $E_g(5)$ (bottom panel) phonon modes of *c*-plane (red and pink for sample S1 and S2, respectively) and *m*-oriented (blue, sample S2) α-In_2O_3 together with the corresponding model fits (dashed lines) based on Eqs. (3)–(6). The error bars indicate the uncertainty of the Raman shift obtained from the Lorentzian fit using Eq. (2) applied to the Raman spectra. Error bars are shown only when they exceed the symbol size. The uncertainty of the temperature values is smaller than the symbol size for all data points.

measurements (blue) tend to have the least temperature shift while the *c*-plane measurements on the same sample (red) tend to have the strongest decrease in wave number with increasing temperature. Also the *m*-oriented measurements show the highest spread. Note that in the $E_g(4)$ mode the data point at 240 K is missing for the *m*-oriented measurements as this was an outlier at a $\sim$383.3 cm^{-1}. We explain this spread by the fact that these measurements were taken on the sample edge which is less smooth than the surface. Also along the *m*-direction we get substantially less signal intensity specifically for the $E_g(4)$ and $E_g(5)$ mode compared to the *c*-direction which of course also increases the experimental uncertainty in their evaluation. In total $E_g(4)$ and $E_g(5)$ modes show similar wave-number shifts with $\sim$2 and $\sim$3 cm^{-1} for the S1 and S2 *c*-plane measurements respectively. This is stronger than the $A_{1g}(1)$ mode shift with $\sim$1.5 and $\sim$2.5 cm^{-1}, respectively. They are therefore only partly in agreement with the shift in α-Al_2O_3 where also the $E_g(5)$ mode had the strongest shift but the $E_g(4)$ mode had the weakest.

The temperature dependence of the phonon frequencies is then as well fitted by the model (dashed line) based on Eqs. (3)–(6), using Table II, to determine the phonon decay factors A and B. The results and their numerical fitting error, of the model-fit in Fig. 7, are listed in Table IV.

C. Phonon decay factors

Tables III and IV list all determined phonon decay factors A and B of α-Al_2O_3 and α-In_2O_3. The values of α-Al_2O_3 are compared to results by Grümbel *et al.* [64] on α-Al_2O_3 (in their supplement) and α-Ga_2O_3. The α-In_2O_3 values are compared to results by Cuscó *et al.* [65]. In all references, the $A_{1g}(1)$ mode has been evaluated as well but other E_g modes were investigated beside those in this work. Also, it has to be noted that a different model was used by Cuscó *et al.* [65] and while it also accounts for thermal expansion in a similar way and the decay into two and three phonons it does not lead to comparable decay factors. Their model describes the phonon shift and the corresponding broadening based on the complex phonon self-energy. For this the two-phonon density of states from density functional perturbation theory is a necessary input. By this, it is definitely the more accurate model, but as this is not applicable in the required accuracy and for all three materials compared here (α-Al_2O_3, α-Ga_2O_3, and α-In_2O_3) it was not used in our work. To still enable comparability we fitted the temperature dependent wave number shifts of Cuscó *et al.* [65] ourselves, using our model, which leads to the values given in Table IV.

When comparing the results, the first thing to note is that for all three materials $|A| > |B|$ is always true. Even more, there is at least one order of magnitude between them, in most cases (14 out of 21 A and B sets) even two orders of magnitude or higher ($|A| \gg |B|$). As A and B are the factors for the decay of one phonon into two and three phonons, respectively (i.e., three- and four-phonon processes) $|A| \gg |B|$ means that the decay into two phonons is by far more dominant that the decay into three. Both A and B increase with the wave number of the corresponding phonon mode (except for the results by Grümbel *et al.* [64]). The reason for this is that a phonon mode of higher wave number has more possible decay channels into phonons of smaller wave number as more such phonons exist. This is also the reason that the same decay factor of the same mode is different between materials. It tends to increase with decreasing atomic mass of the metal. For example, the absolute value of A of the $A_{1g}(1)$ mode of α-Al_2O_3 is always higher than that of α-In_2O_3. The $A_{1g}(1)$ mode of α-Al_2O_3 is at a higher wave number and has the $E_g(1)$ mode (along with and several acoustical modes) below it as a

TABLE III. Phonon decay factors A and B and their corresponding numerical errors of the decay into two and three phonons, respectively, are listed for different phonon modes of α-Al_2O_3 based on $z(x,-)\bar{z}$ measurements on a c-plane wafer and $x(y,-)\bar{x}$ measurements on an m-plane wafer in comparison to results of c-plane α-Al_2O_3 and m-oriented (edge measurement of a c-plane layer) α-Ga_2O_3 by Grümbel *et al.* [64].

	α-Al_2O_3			α-Ga_2O_3
	c-plane		m-plane	m-oriented
	This work	Ref. [64]	This work	Ref. [64]
$A_{1g}(1)$ (418 cm^{-1})				(221 cm^{-1})
A (cm^{-1})	-0.068 ± 0.013	-0.160 ± 0.007	-0.052 ± 0.006	-0.068 ± 0.007
B (cm^{-1})	$(-8 \pm 8) \times 10^{-4}$	$(7 \pm 2) \times 10^{-4}$	$(-2.7 \pm 0.3) \times 10^{-3}$	$(2 \pm 20) \times 10^{-6}$
$E_g(1)$ (379 cm^{-1})				
A (cm^{-1})		-0.045 ± 0.009		
B (cm^{-1})		$(7 \pm 2) \times 10^{-4}$		
$E_g(2)$ (431 cm^{-1})				(289 cm^{-1})
A (cm^{-1})				-0.06 ± 0.01
B (cm^{-1})				$(4 \pm 20) \times 10^{-5}$
$E_g(4)$ (578 cm^{-1})				
A (cm^{-1})	-0.17 ± 0.01		-0.149 ± 0.004	
B (cm^{-1})	$(9.1 \pm 0.9) \times 10^{-3}$		$(6.6 \pm 0.3) \times 10^{-3}$	
$E_g(5)$ (751 cm^{-1})				
A (cm^{-1})	-0.23 ± 0.056		-0.25 ± 0.016	
B (cm^{-1})	0.012 ± 0.006		0.012 ± 0.0016	

potential decay channel, while the $A_{1g}(1)$ mode of α-In_2O_3 is not only at a lower wave numbers but also the lowest optical mode, as the $A_{1g}(1)$ and $E_g(1)$ modes cross between these materials.

In almost all cases, $A < 0$ is true while $B < 0$ only in the case of A_{1g} modes (again except for the results by Grümbel *et al.* [64]) while all E_g modes have $B > 0$. All in all, only looking at modes were more than one A and B data set exists, A as well as B of the same mode but of different samples, or orientations match reasonable well with each other. The B values tend to differ stronger from each other than the A values which is not surprising as they describe a weaker phenomenon. The only notable exception in terms of the A factor is the A value of the $A_{1g}(1)$ mode in α-Al_2O_3, which differs between our c-plane sample ($-0.068\,cm^{-1}$) and that of Grümbel *et al.* [64] ($-0.16\,cm^{-1}$). This could potentially be related to differences in the specific sample conditions, given the several years between the studies, or variations between the samples themselves. On the other hand, especially the A values of the $E_g(5)$ mode match very well with each other for all samples/orientations of α-Al_2O_3 and α-In_2O_3.

TABLE IV. Phonon decay factors A and B and their corresponding numerical errors of the decay into two and three phonons, respectively, are listed for different phonon modes of α-In_2O_3 based on $z(x,-)\bar{z}$ (c-plane) measurements on two samples (S1 and S2) and $x(y,-)\bar{x}$ (m-oriented, edge measurement) measurements on sample S2 in comparison to results by Cuscó *et al.* [65].

	α-In_2O_3			
	c-plane			m-oriented
	This work, S1	This work, S2	Ref. [65]	This work, S2
$A_{1g}(1)$ (164 cm^{-1})				
A (cm^{-1})	0.002 ± 0.003	-0.029 ± 0.006	-0.022 ± 0.003	-0.013 ± 0.003
B (cm^{-1})	$(-7.2 \pm 0.8) \times 10^{-4}$	$(-7 \pm 1.4) \times 10^{-4}$	$(-2.9 \pm 0.4) \times 10^{-4}$	$(-3.6 \pm 0.7) \times 10^{-4}$
$A_{1g}(2)$ (504 cm^{-1})				
A (cm^{-1})			-0.18 ± 0.018	
B (cm^{-1})			$(-3.1 \pm 0.7) \times 10^{-3}$	
$E_g(4)$ (386 cm^{-1})				
A (cm^{-1})	-0.09 ± 0.021	-0.13 ± 0.014		-0.18 ± 0.036
B (cm^{-1})	$(2 \pm 1) \times 10^{-3}$	$(9 \pm 7.6) \times 10^{-4}$		$(8 \pm 2) \times 10^{-3}$
$E_g(5)$ (593 cm^{-1})				
A (cm^{-1})	-0.22 ± 0.03	-0.25 ± 0.03		-0.27 ± 0.08
B (cm^{-1})	0.014 ± 0.003	$(9 \pm 3) \times 10^{-3}$		0.026 ± 0.007

IV. SUMMARY

To recapitulate, α-In_2O_3 and α-Al_2O_3 were analyzed by temperature dependent Raman spectroscopy to determine the phonon decay factors A and B of the decay into two and three phonons, respectively. c-plane and m-plane α-Al_2O_3 wafers as well as two different c-plane α-In_2O_3 thin film samples on α-Al_2O_3 substrates, oriented along the c- and the m-direction, were measured by temperature dependent Raman spectroscopy between 80 and 300 K. The signals of the Raman active phonon modes $A_{1g}(1)$, $E_g(4)$, and $E_g(5)$ were fitted by Lorentzian line shapes. The shift of their resonance frequencies with increasing temperature was analyzed by a model taking into account the thermal expansion of the lattice and the decay of the phonons. The resulting phonon decay factors were discussed and compared to literature results on α-Al_2O_3 and α-In_2O_3, as well as α-Ga_2O_3. By quantifying phonon decay processes in α-In_2O_3 and α-Al_2O_3 this work contributes significantly to understanding the thermal properties of corundum structured semiconductors, essential for developing efficient optoelectronic and power electronic devices.

ACKNOWLEDGMENTS

This work was funded by the EU EFRE funding under Contract No. ZS/2023/12/182333. We would like to acknowledge Jürgen Bläsing (Otto-von-Guericke-Universität Magdeburg) for the determination of the lattice parameters.

Work distribution: Raman spectroscopy and evaluation: J.E.M.; Mist CVD growth: A.T., T.Y.; Hall effect measurements: T.Y.; Ellipsometry measurements: E.K.; Writing - Original draft: E.K.; Writing - Review and Editing: E.K., J.E.M., T.Y., M.F., R.G.; Supervision: E.K., M.F., R.G.; Funding and administration: M.F., R.G.

The authors have no conflict of interest to disclose.

DATA AVAILABILITY

The data that support the findings of this article are not publicly available upon publication because it is not technically feasible and/or the cost of preparing, depositing, and hosting the data would be prohibitive within the terms of this research project. The data are available from the authors upon reasonable request.

[1] T. Koida, H. Fujiwara, and M. Kondo, High-mobility hydrogen-doped In_2O_3 transparent conductive oxide for a-Si:H/c-Si heterojunction solar cells, Sol. Energy Mater. Sol. Cells **93**, 851 (2009).

[2] O. Bierwagen, Indium oxide—a transparent, wide-band gap semiconductor for (opto)electronic applications, Semicond. Sci. Technol. **30**, 024001 (2015).

[3] Indium tin oxide (ITO) thin films: Fabrication, properties, post-deposition, trends in semiconductor research, *Trends in Semiconductor Research*, edited by T. B. Elliot (Nova Science Publishers, New York, 2005), pp. 1–32.

[4] P. Lippens and U. Muehlfeld, Indium tin oxide (ITO): Sputter deposition processes, in *Handbook of Visual Display Technology*, edited by J. Chen, W. Cranton, and M. Fihn (Springer, Berlin, 2012), pp. 779–794

[5] Y. Shigesato, In based TCOs, in *Handbook of Transparent Conductors*, edited by D. S. Ginley (Springer US, Boston, 2011), pp. 149–169.

[6] K. Ellmer, R. Mientus, and S. Seeger, Metallic oxides (ITO, ZnO, SnO_2, TiO_2), in *Transparent Conductive Materials* (Wiley, Weinheim, Germany, 2018), Chap. 2.1, pp. 31–80.

[7] J. A. Spencer, A. L. Mock, A. G. Jacobs, M. Schubert, Y. Zhang, and M. J. Tadjer, A review of band structure and material properties of transparent conducting and semiconducting oxides: Ga_2O_3, Al_2O_3, In_2O_3, ZnO, SnO_2, CdO, NiO, CuO, and Sc_2O_3, Appl. Phys. Rev. **9**, 011315 (2022).

[8] I. Hamberg and C. G. Granqvist, Evaporated Sn-doped In_2O_3 films: Basic optical properties and applications to energy-efficient windows, J. Appl. Phys. **60**, R123 (1986).

[9] J. S. Lee, Y.-J. Kwack, and W.-S. Choi, Inkjet-printed In_2O_3 thin-film transistor below 200°C, ACS Appl. Mater. Interfaces **5**, 11578 (2013).

[10] Z. Yuan, X. Zhu, X. Wang, X. Cai, B. Zhang, D. Qiu, and H. Wu, Annealing effects of In_2O_3 thin films on electrical properties and application in thin film transistors, Thin Solid Films **519**, 3254 (2011).

[11] P. K. Nayak, M. N. Hedhili, D. Cha, and H. N. Alshareef, High performance In_2O_3 thin film transistors using chemically derived aluminum oxide dielectric, Appl. Phys. Lett. **103**, 033518 (2013).

[12] J. Michel, D. Splith, J. Rombach, A. Papadogianni, T. Berthold, S. Krischok, M. Grundmann, O. Bierwagen, H. von Wenckstern, and M. Himmerlich, Processing strategies for high-performance Schottky contacts on n-type oxide semiconductors: Insights from In_2O_3, ACS Appl. Mater. Interfaces **11**, 27073 (2019).

[13] H. von Wenckstern, D. Splith, F. Schmidt, M. Grundmann, O. Bierwagen, and J. S. Speck, Schottky contacts to In_2O_3, APL Mater. **2**, 046104 (2014).

[14] J.-H. Kim, H.-J. Seok, H.-J. Seo, T.-Y. Seong, J. H. Heo, S.-H. Lim, K.-J. Ahn, and H.-K. Kim, Flexible ITO films with atomically flat surfaces for high performance flexible perovskite solar cells, Nanoscale **10**, 20587 (2018).

[15] R. Sharma, R. S. Mane, S.-K. Min, and S.-H. Han, Optimization of growth of In_2O_3 nano-spheres thin films by electrodeposition for dye-sensitized solar cells, J. Alloys Compd. **479**, 840 (2009).

[16] M. Himmerlich, C. Y. Wang, V. Cimalla, O. Ambacher, and S. Krischok, Surface properties of stoichiometric and defect-rich indium oxide films grown by MOCVD, J. Appl. Phys. **111**, 093704 (2012).

[17] C. W. Tang and S. A. VanSlyke, Organic electroluminescent diodes, Appl. Phys. Lett. **51**, 913 (1987).

[18] M. T. Hardy, C. O. Holder, D. F. Feezell, S. Nakamura, J. S. Speck, D. A. Cohen, and S. P. DenBaars, Indium-tin-oxide clad blue and true green semipolar InGaN/GaN laser diodes, Appl. Phys. Lett. **103**, 081103 (2013).

[19] M. Feneberg, J. Nixdorf, C. Lidig, R. Goldhahn, Z. Galazka, O. Bierwagen, and J. S. Speck, Many-electron effects on the

dielectric function of cubic In_2O_3: Effective electron mass, band nonparabolicity, band gap renormalization, and Burstein-Moss shift, Phys. Rev. B **93**, 045203 (2016).

[20] C. Kranert, R. Schmidt-Grund, and M. Grundmann, Raman active phonon modes of cubic In_2O_3, Phys. Rapid Res. Lett. **8**, 554 (2014).

[21] D. Kim and S. Lee, Persistent metallic Sn-doped In_2O_3 epitaxial ultrathin films with enhanced infrared transmittance, Sci. Rep. **10**, 4957 (2020).

[22] K. O. Egbo, A. E. Adesina, C. V. Ezeh, C. P. Liu, and K. M. Yu, Effects of free carriers on the optical properties of high mobility transition metal doped In_2O_3 transparent conductors, Phys. Rev. Mater. **5**, 094603 (2021).

[23] P. D. C. King, T. D. Veal, D. J. Payne, A. Bourlange, R. G. Egdell, and C. F. McConville, Surface electron accumulation and the charge neutrality level in In_2O_3, Phys. Rev. Lett. **101**, 116808 (2008).

[24] M. Ramsteiner, J. Feldl, and Z. Galazka, Signatures of free carriers in Raman spectra of cubic In_2O_3, Semicond. Sci. Technol. **35**, 015017 (2020).

[25] A. Klein, A. Frebel, K. A. Creutz, and B. Huang, Origin and quantification of the ultimate carrier concentration limits in In_2O_3 and Sn-doped In_2O_3, Phys. Rev. Mater. **8**, 044601 (2024).

[26] C. Körber, V. Krishnakumar, A. Klein, G. Panaccione, P. Torelli, A. Walsh, J. L. F. Da Silva, S.-H. Wei, R. G. Egdell, and D. J. Payne, Electronic structure of In_2O_3 and Sn-doped In_2O_3 by hard X-ray photoemission spectroscopy, Phys. Rev. B **81**, 165207 (2010).

[27] K. H. L. Zhang, R. G. Egdell, F. Offi, S. Iacobucci, L. Petaccia, S. Gorovikov, and P. D. C. King, Microscopic origin of electron accumulation in In_2O_3, Phys. Rev. Lett. **110**, 056803 (2013).

[28] L. Xu, B. Fauqué, Z. Zhu, Z. Galazka, K. Irmscher, and K. Behnia, Thermal conductivity of bulk In_2O_3 single crystals, Phys. Rev. Mater. **5**, 014603 (2021).

[29] D. R. Hagleitner, M. Menhart, P. Jacobson, S. Blomberg, K. Schulte, E. Lundgren, M. Kubicek, J. Fleig, F. Kubel, C. Puls, A. Limbeck, H. Hutter, L. A. Boatner, M. Schmid, and U. Diebold, Bulk and surface characterization of In_2O_3(001) single crystals, Phys. Rev. B **85**, 115441 (2012).

[30] I. Chatratin, F. P. Sabino, P. Reunchan, S. Limpijumnong, J. B. Varley, C. G. Van de Walle, and A. Janotti, Role of point defects in the electrical and optical properties of In_2O_3, Phys. Rev. Mater. **3**, 074604 (2019).

[31] P. Agoston and K. Albe, Thermodynamic stability, stoichiometry, and electronic structure of bcc-In_2O_3 surfaces, Phys. Rev. B **84**, 045311 (2011).

[32] M. F. Bekheet, M. R. Schwarz, S. Lauterbach, H.-J. Kleebe, P. Kroll, R. Riedel, and A. Gurlo, Orthorhombic In_2O_3: A metastable polymorph of indium sesquioxide, Angew. Chem. Int. Ed. **52**, 6531 (2013).

[33] T. de Boer, M. F. Bekheet, A. Gurlo, R. Riedel, and A. Moewes, Band gap and electronic structure of cubic, rhombohedral, and orthorhombic In_2O_3 polymorphs: Experiment and theory, Phys. Rev. B **93**, 155205 (2016).

[34] F. Komine, M. Tomic, T. Gerds, and J. R. Strub, Influence of different adhesive resin cements on the fracture strength of aluminum oxide ceramic posterior crowns, J. Prosthet. Dent. **92**, 359 (2004).

[35] C.-W. Chang and C.-P. Kuo, Evaluation of surface roughness in laser-assisted machining of aluminum oxide ceramics with Taguchi method, Int. J. Mach. Tools Manufacture **47**, 141 (2007).

[36] E. Richter, C. Hennig, M. Weyers, F. Habel, J.-D. Tsay, W.-Y. Liu, P. Brückner, F. Scholz, Y. Makarov, A. Segal, and J. Kaeppeler, Reactor and growth process optimization for growth of thick GaN layers on sapphire substrates by HVPE, J. Cryst. Growth **277**, 6 (2005).

[37] K. Hiramatsu, H. Amano, I. Akasaki, H. Kato, N. Koide, and K. Manabe, MOVPE growth of GaN on a misoriented sapphire substrate, J. Cryst. Growth **107**, 509 (1991).

[38] Y. Cheng, Y. Xu, Z. Li, J. Zhang, D. Chen, Q. Feng, S. Xu, H. Zhou, J. Zhang, Y. Hao, and C. Zhang, Heteroepitaxial growth of α-Ga_2O_3 thin films on a-, c- and r-plane sapphire substrates by low-cost mist-CVD method, J. Alloys Compd. **831**, 154776 (2020).

[39] D. Yang, B. Kim, T. H. Eom, Y. Park, and H. W. Jang, Epitaxial growth of alpha gallium oxide thin films on sapphire substrates for electronic and optoelectronic devices: Progress and perspective, Electron. Mater. Lett. **18**, 113 (2022).

[40] S. Fujita and K. Kaneko, Epitaxial growth of corundum-structured wide band gap III-oxide semiconductor thin films, J. Cryst. Growth **401**, 588 (2014).

[41] S. Fujita, M. Oda, K. Kaneko, and T. Hitora, Evolution of corundum-structured III-oxide semiconductors: Growth, properties, and devices, Jpn. J. Appl. Phys. **55**, 1202A3 (2016).

[42] R. Cuscó, T. Yamaguchi, E. Kluth, R. Goldhahn, and M. Feneberg, Optical properties of corundum-structured In_2O_3, Appl. Phys. Lett. **121**, 062106 (2022).

[43] A. K. Harman, S. Ninomiya, and S. Adachi, Optical constants of sapphire ($\alpha - Al_2O_3$) single crystals, J. Appl. Phys. **76**, 8032 (1994).

[44] D. D. Minh, N. L. M. An, K.-H. Kim, S.-Y. Bae, and M.-T. Ha, Corundum $(In_xGa_{1-x})_2O_3$ alloys: First-principles study, epitaxial growth and thermal annealing, ChemPhysMater **5**, 232 (2026).

[45] B. K. C. Bhupendra, V. Barone, S. Kandel, M. Sitaula, B. Dumre, R. Ellingson, and S. Khare, Computational investigation of structural, electronic, and optical properties of $(In_xGa_{1-x})_2O_3$ alloys as candidates for emitter layer application in solar cells, Physica B **715**, 417615 (2025).

[46] M. S. Williams, M. Alonso-Orts, M. Schowalter, A. Karg, S. Raghuvansy, J. P. McCandless, D. Jena, A. Rosenauer, M. Eickhoff, and P. Vogt, Growth, catalysis, and faceting of α-Ga_2O_3 and α-$(In_xGa_{1-x})_2O_3$ on m-plane α-Al_2O_3 by molecular beam epitaxy, APL Mater. **12**, 011120 (2024).

[47] E. Kluth, M. Fay, C. Parmenter, J. Roberts, E. Smith, C. Stoppiello, F. Massabuau, R. Goldhahn, and M. Feneberg, Redshift and amplitude increase in the dielectric function of corundum-like α-$(Ti_xGa_{1-x})_2O_3$, Appl. Phys. Lett. **122**, 092101 (2023).

[48] S.-i. Kan, S. Takemoto, K. Kaneko, I. Takahashi, M. Sugimoto, T. Shinohe, and S. Fujita, Electrical properties of α-Ir_2O_3/α-Ga_2O_3 pn heterojunction diode and band alignment of the heterostructure, Appl. Phys. Lett. **113**, 212104 (2018).

[49] K. Kaneko, S. Fujita, T. Shinohe, and K. Tanaka, Progress in α-Ga_2O_3 for practical device applications, Jpn. J. Appl. Phys. **62**, SF0803 (2023).

[50] S. Khalid and A. Janotti, Electronic properties of corundum-like Ir_2O_3 and Ir_2O_3-Ga_2O_3 alloys, Appl. Phys. Lett. **125**, 202102 (2024).

[51] P. D. C. King, T. D. Veal, F. Fuchs, C. Y. Wang, D. J. Payne, A. Bourlange, H. Zhang, G. R. Bell, V. Cimalla, O. Ambacher, R. G. Egdell, F. Bechstedt, and C. F. McConville, Band gap, electronic structure, and surface electron accumulation of cubic and rhombohedral In_2O_3, Phys. Rev. B **79**, 205211 (2009).

[52] F. Fuchs and F. Bechstedt, Indium-oxide polymorphs from first principles: Quasiparticle electronic states, Phys. Rev. B **77**, 155107 (2008).

[53] C. Ribeiro da Silva, F. Bechstedt, L. Kühl Teles, and M. Marques, Electronic and optical properties of highly complex Ga_2O_3 and In_2O_3 polymorphs using approximate quasiparticle dft + A – 1/2, J. Phys. Chem. C **129**, 3179 (2025).

[54] C. Y. Wang, V. Cimalla, H. Romanus, T. Kups, G. Ecke, T. Stauden, M. Ali, V. Lebedev, J. Pezoldt, and O. Ambacher, Phase selective growth and properties of rhombohedral and cubic indium oxide, Appl. Phys. Lett. **89**, 011904 (2006).

[55] C. Wang, V. Cimalla, H. Romanus, T. Kups, M. Niebelschütz, and O. Ambacher, Tuning of electrical and structural properties of indium oxide films grown by metal organic chemical vapor deposition, Thin Solid Films **515**, 6611 (2007).

[56] K. H. L. Zhang, V. K. Lazarov, P. L. Galindo, F. E. Oropeza, D. J. Payne, H. H.-C. Lai, and R. G. Egdell, Domain matching epitaxial growth of In_2O_3 thin films on α-Al_2O_3(0001), Cryst. Growth Design **12**, 1000 (2012).

[57] H. Nishinaka and M. Yoshimoto, Mist chemical vapor deposition of single-phase metastable rhombohedral indium tin oxide epitaxial thin films with high electrical conductivity and transparency on various α-Al_2O_3 substrates, Cryst. Growth Design **18**, 4022 (2018).

[58] T. Yamaguchi, S. Takahashi, T. Kiguchi, A. Sekiguchi, K. Kaneko, S. Fujita, H. Nagai, M. Sato, T. Onuma, and T. Honda, Impact of hydrochloric acid on the epitaxial growth of In_2O_3 films on (0001)α-Al_2O_3 substrates by mist CVD, Appl. Phys. Express **13**, 075504 (2020).

[59] A. Taguchi, S. Takahashi, A. Sekiguchi, K. Kaneko, S. Fujita, T. Onuma, T. Honda, and T. Yamaguchi, Mist chemical vapor deposition growth of α-In_2O_3 films using indium oxide powder as source precursor, Phys. Status Solidi B **259**, 2100414 (2022).

[60] A. Taguchi, T. Yamamoto, K. Kaneko, K. Goto, T. Onuma, T. Honda, Y. Kumagai, S. Fujita, and T. Yamaguchi, Growth of α-In_2O_3 films with different concentrations of In_2O_3 powder used as source precursor by mist chemical vapor deposition, Jpn. J. Appl. Phys. **62**, SF1023 (2023).

[61] B. García-Domene, J. A. Sans, F. J. Manjón, S. V. Ovsyannikov, L. S. Dubrovinsky, D. Martinez-Garcia, O. Gomis, D. Errandonea, H. Moutaabbid, Y. Le Godec, H. M. Ortiz, A. Muñoz, P. Rodríguez-Hernández, and C. Popescu, Synthesis and high-pressure study of corundum-type In_2O_3, J. Phys. Chem. C **119**, 29076 (2015).

[62] F. Liu, P. Parajuli, R. Rao, P. C. Wei, A. Karunarathne, S. Bhattacharya, R. Podila, J. He, B. Maruyama, G. Priyadarshan, J. R. Gladden, Y. Y. Chen, and A. M. Rao, Phonon anharmonicity in single-crystalline SnSe, Phys. Rev. B **98**, 224309 (2018).

[63] B. Wei, Q. Sun, C. Li, and J. Hong, Phonon anharmonicity: A pertinent review of recent progress and perspective, Sci. China Phys. Mech. Astron. **64**, 117001 (2021).

[64] J. Grümbel, R. Goldhahn, D.-W. Jeon, and M. Feneberg, Anharmonicity of lattice vibrations in thin film α-Ga_2O_3 investigated by temperature dependent Raman spectroscopy, Appl. Phys. Lett. **120**, 022104 (2022).

[65] R. Cuscó, A. Taguchi, and T. Yamaguchi, Phonon anharmonicity in α-In_2O_3: A Raman scattering study of the A_{1g} modes, J. Alloys Compd. **1020**, 179350 (2025).

[66] A. Schauer, Thermal expansion, Grueneisen parameter, and temperature dependence of lattice vibration frequencies of aluminum oxide, Can. J. Phys. **43**, 523 (1965).

[67] S. P. S. Porto and R. S. Krishnan, Raman effect of corundum, J. Chem. Phys. **47**, 1009 (1967).

[68] R. Cuscó, N. Domènech-Amador, T. Hatakeyama, T. Yamaguchi, T. Honda, and L. Artús, Lattice dynamics of a mist-chemical vapor deposition-grown corundum-like Ga_2O_3 single crystal, J. Appl. Phys. **117**, 185706 (2015).

[69] See Supplemental Material at http://link.aps.org/supplemental/10.1103/vxv3-wrh3 for visualizations of the Raman active phonon modes $A_{1g}(1)$, $E_g(4)$, and $E_g(5)$, which includes Refs. [42,73].

[70] A. Link, K. Bitzer, W. Limmer, R. Sauer, C. Kirchner, V. Schwegler, M. Kamp, D. G. Ebling, and K. W. Benz, Temperature dependence of the E_2 and A_1(LO) phonons in GaN and AlN, J. Appl. Phys. **86**, 6256 (1999).

[71] M. Balkanski, R. F. Wallis, and E. Haro, Anharmonic effects in light scattering due to optical phonons in silicon, Phys. Rev. B **28**, 1928 (1983).

[72] J. Feldl, M. Feneberg, A. Papadogianni, J. Lähnemann, T. Nagata, O. Bierwagen, R. Goldhahn, and M. Ramsteiner, Bandgap widening and behavior of Raman-active phonon modes of cubic single-crystalline $(In, Ga)_2O_3$ alloy films, Appl. Phys. Lett. **119**, 042101 (2021).

[73] A. Kokalj, XCrySDen - a new program for displaying crystalline structures and electron densities, J. Mol. Graphics Modell. **17**, 176 (1999).